JOURNAL OF GUIDANCE, CONTROL, AND DYNAMICS
Vol. 30, No. 2, March–April 2007

Feasible Trajectory Generation for Atmospheric Entry Guidance

James A. Leavitt* and Kenneth D. Mease†
University of California, Irvine, California 92697

DOI: 10.2514/1.23034

An atmospheric entry trajectory planner is developed that generates a feasible trajectory and associated bank angle profile. Feasibility denotes that the initial and final state conditions, the path and control constraints, and the nominal equations of motion are all satisfied. Feasible trajectories are easier to track, and thus enhanced performance is expected when the trajectory planner is combined with a tracking law for entry guidance. Insights from computing maximum crossrange trajectories are factored into the design of the planner, and as a result that it can generate trajectories to most of the landing footprint. Drag profile design is central in the planning approach, but in addition both longitudinal and lateral motions are accounted for, including bank reversal planning, and the assumption of zero flight path angle is not required. Comparisons of trajectories created by the new planner and optimal trajectories and guidance simulation results using an algorithm based on the new planner demonstrate the performance improvements.

Nomenclature

$A_{\max}$	=	maximum allowable normal acceleration, ft/s^2
C_D	=	coefficient of drag
C_L	=	coefficient of lift
C_γ	=	Coriolis acceleration term in γ' equation, rad $\cdot$ s^2/ft^2
C_ψ	=	Coriolis acceleration term in ψ' equation, rad $\cdot$ s^2/ft^2
D	=	drag acceleration, ft/s^2
$D_{\text{e.g.}}$	=	equilibrium glide drag boundary, ft/s^2
$D_{\max}$	=	vehicle constraint upper drag boundary, ft/s^2
$D_{\max f}$	=	feasible upper drag boundary, ft/s^2
$D_{\min f}$	=	feasible lower drag boundary, ft/s^2
D_{ref}	=	reference drag profile, ft/s^2
E	=	energy divided by vehicle mass, ft/s^2
$\tilde{E}$	=	normalized energy
$\tilde{E}_m$	=	drag interpolation shaping parameter
g	=	gravitational acceleration, ft/s^2
h	=	altitude, ft
h_s	=	scale height, ft
k_1	=	integral gain in drag tracking law
k_2	=	proportional gain in heading angle tracking law
k_3	=	integral gain in heading angle tracking law
L	=	lift acceleration, ft/s^2
L_n	=	normal acceleration, ft/s^2
M	=	Mach number
m	=	vehicle mass, slugs
P_1	=	normalized downrange parameter
P_2	=	normalized crossrange parameter
Q	=	heat load, BTU/ft^2
$\dot{Q}$	=	thermal flux, BTU/ft^2/s
$\bar{q}$	=	dynamic pressure, lbf/ft^2
r	=	radial distance from vehicle to planet center, ft
r_{eq}	=	planet surface radius at equator, ft
S	=	reference wing area, ft^2
t	=	time, s
V	=	planet-relative speed, ft/s
α	=	angle of attack, rad
γ	=	flight path angle, rad
ζ	=	damping ratio of desired drag error dynamics
θ	=	longitude, rad
μ	=	gravitational constant, ft^3/s^2
ρ	=	atmospheric density, slugs/ft^3
ρ_{eq}	=	atmospheric density at r_{eq}, slugs/ft^3
σ	=	bank angle, rad
ϕ	=	latitude, rad
ψ	=	heading angle with $\psi = 0$ as due east, rad
ψ_{ref}	=	reference heading angle profile, rad
ω_n	=	natural frequency of desired drag error dynamics, rad/s
ω_p	=	angular rate of planet rotation, rad/s

Introduction

TO reduce cost and increase safety, a goal for next generation reusable launch vehicles (RLVs) is aircraftlike operation. To realize this goal requires advances in entry guidance [1]. An entry guidance algorithm determines, repetitively during entry, the bank angle profile, and if appropriate also the angle of attack profile, required to steer the vehicle to the desired landing site. In the context of the entry guidance problem, one or both of these angles are considered to be the controls. The equations of motion relating the control profiles to the vehicle position and velocity are nonlinear and must be based on vehicle and atmospheric models that are inaccurate. The position and velocity inputs to the guidance algorithm will also be inaccurate. The guidance problem that the algorithm solves is further complicated by the need to respect path constraints on vehicle heating, acceleration and dynamic pressure, and control constraints on the bank angle and angle of attack. Most guidance algorithms operate with a reference trajectory. Although for vehicles with a limited flight envelope and focused mission it is adequate to have the trajectory generator on the ground, on-board trajectory generation is arguably a requirement for RLVs to achieve aircraftlike operation for the entire set of nominal and abort mission scenarios.

The state-of-the-art operational entry guidance is embodied in the entry guidance algorithm for the U.S. Space Shuttle Orbiter [2]. The algorithm is composed of a trajectory planning function and a trajectory tracking function. Much of the complexity and uncertainty of the entry trajectory planning problem is circumvented by using the drag acceleration as a surrogate control variable. The path constraints and final altitude constraint are converted to drag constraints. Assuming flight on a great circle arc to the target longitude and latitude to determine the required range, a drag profile satisfying the

Received 9 February 2006; revision received 26 May 2006; accepted for publication 3 June 2006.

*Graduate Research Assistant, Department of Mechanical and Aerospace Engineering; jleavitt@uci.edu.

†Professor, Department of Mechanical and Aerospace Engineering; kmease@uci.edu. Associate Fellow AIAA.

constraints and producing the required range is planned. With energy as the independent variable, determining range for a drag profile requires the integration of a scalar first-order differential equation. This differential equation under the given assumptions is an exact kinematic relation between drag and the derivative of range with respect to energy. A drag tracking law specifies the magnitude of the bank angle. The sign of the bank angle is determined by a heading error corridor. In the Shuttle entry guidance only the longitudinal motion is considered in the planning. Various authors [3–7] have proposed and evaluated potential improvements to the Shuttle entry guidance; in each case the planning is limited to the longitudinal motion.

To achieve aircraftlike operation and the capability of "returning the vehicle safely in any situation where this is physically possible" [1], future RLVs will need to fly trajectories that differ significantly from great circle arcs and have a guidance algorithm that can plan and execute such trajectories. The Shuttle trajectory planning strategy has been extended [8,9] to combined longitudinal and lateral motion planning. By making two mild approximations [8], the planning requires the integration of only three first-order differential equations. The altitude and flight path angle dynamics are eliminated, which, in addition to order reduction, avoids the sensitivity in planning due to phugoidlike motion. The complexity of the planning problem is further reduced by breaking the problem into two subproblems and using a successive approximation approach. The longitudinal subproblem is essentially the drag planning problem solved in the Shuttle guidance, except that the great circle arc assumption has been eliminated. By solving the lateral subproblem, bank reversals are planned and the curved path to the target is computed. Accounting for the curvature allows the drag profile to be planned more accurately, which is especially important for high-crossrange targets. The planner was combined with a tracking law to construct an entry guidance algorithm referred to as evolved acceleration guidance logic for entry (EAGLE) [9]. The trajectory planner is fast enough that trajectory replanning to correct for the effects of tracking errors can be part of the real-time guidance strategy. EAGLE can deliver an entry vehicle to the start of a terminal area energy management (TAEM) phase, as does the Shuttle guidance, or it can deliver to a parachute deploy point. Extensive simulation testing results for EAGLE are presented in Saraf et al. [9]. EAGLE performed extremely well in an independently conducted evaluation [10] of several entry guidance algorithms.

In this paper we present a new trajectory planner that possesses near-maximum downrange and crossrange capabilities and that addresses certain limitations of the previous EAGLE planner. The construction of the drag profile in the Shuttle entry planning and in the previous EAGLE entry planning does not take into account the control capability. As a result, a drag profile can be constructed that is difficult to track and the guidance accuracy will suffer. In the EAGLE testing mentioned above, despite the overall excellent performance, tracking difficulties were observed in some suborbital abort cases. The entry guidance of low L/D capsules, such as those used for Mars landing, presents a more serious challenge for drag planning, because of the very limited control authority. Numerical integration with a constant intermediate bank angle has been used to generate an initial drag profile [6]. A different approach to constructing a more easily tracked drag profile is presented in this paper. Interpolation and pretracking are used to reduce the complexity of the drag planning, yet produce a flyable drag profile. Pretracking begins with a trajectory generated by some means that neglects certain constraints or uses approximations to the equations of motion to simplify the trajectory computation. A simulation is then run in which the initial trajectory is tracked, using some control law, with some or all of the previously neglected constraints and modeling details included. Pretracking has been used previously by Mease et al. [8] and Lu and Shen [11,12]. The new planner matches the vehicle's initial flight path angle and bank angle and enforces the full three-degree-of-freedom (3-DOF) equations of motion with control derivative limits. These improvements increase the likelihood that the planned trajectory can be accurately tracked. In addition, the new planner is not based on the assumption of a small flight path angle.

The purpose of this paper is to present the new entry trajectory planning approach and demonstrate the beneficial features of this approach. The performance of the new planner is demonstrated both separately and as the planning function in EAGLE, replacing the original planner. Testing and validation under a broad range of conditions is outside the scope of this paper. Other approaches to entry guidance can be found in the papers [11–19] and the references therein.

Entry Guidance Problem Formulation

The entry guidance problem considered here is to determine for a given initial state the α and σ commands throughout the entry such that the vehicle path constraints, control constraints, and the final conditions are satisfied. This section describes the formulation and supporting models. Because the focus of this paper is trajectory planning, we do not explicitly address modeling or navigation uncertainties, except briefly in the Results section. EAGLE has been shown to adequately accommodate these important aspects of the guidance problem in other work [8–10].

Entry Dynamics

The translational dynamics of an atmospheric entry vehicle are defined with respect to a planet-fixed coordinate frame and with E as the independent variable. $E = V^2/2 - \mu/r$. With energy as the independent variable, the vehicle's translational motion can be modeled by five differential equations. The control variables are taken to be bank angle σ and angle of attack α. Angle of attack appears in the equations of motion through lift and drag, whereas bank angle appears explicitly. Neglecting winds and centripetal acceleration from planet rotation, the equations of motion, consistent with those given in [20] except for the transformation to energy as the independent variable, are

$$\begin{aligned}
\theta' &= -\frac{\cos\gamma\cos\psi}{r\cos\phi}\left(\frac{1}{D}\right) \qquad \phi' = -\frac{\cos\gamma\sin\psi}{r}\left(\frac{1}{D}\right)\\
r' &= -\sin\gamma\left(\frac{1}{D}\right)\\
\psi' &= \frac{\cos\psi\tan\phi\cos\gamma}{r}\left(\frac{1}{D}\right) + \frac{1}{V^2\cos\gamma}\left(\frac{L\sin\sigma}{D}\right) + \mathcal{C}_\psi\\
\gamma' &= \left(g - \frac{V^2}{r}\right)\frac{\cos\gamma}{V^2}\left(\frac{1}{D}\right) - \frac{1}{V^2}\left(\frac{L}{D}\cos\sigma\right) + \mathcal{C}_\gamma
\end{aligned} \tag{1}$$

Both γ and ψ describe the orientation of the planet-relative velocity vector. σ is defined such that a bank to the right is positive and zero bank corresponds to the lift vector directed upward in the longitudinal plane. Initial control and state variable values will be denoted with subscript "0", whereas target state values will be denoted with subscript "f". The lift L and drag D accelerations are given by

$$L = \frac{1}{2}\rho(r)V^2\cdot\frac{S}{m}\cdot C_L(\alpha, M) \qquad D = \frac{1}{2}\rho(r)V^2\cdot\frac{S}{m}\cdot C_D(\alpha, M) \tag{2}$$

where $\rho(r)$ is the density as a function of altitude, $C_L(\alpha, M)$ and $C_D(\alpha, M)$ are the lift and drag coefficients as functions of α and M. Specific gravity is modeled as $g = \mu/r^2$. The density variation with altitude is modeled using the exponential equation

$$\rho(r) = \rho_{\text{eq}}e^{-(r-r_{\text{eq}})/h_s} \tag{3}$$

The terms $\mathcal{C}_\psi$ and $\mathcal{C}_\gamma$ are given as

$$\begin{aligned}
\mathcal{C}_\psi &= -\left(\frac{2\omega_p}{VD}\right)(\tan\gamma\sin\psi\cos\phi - \sin\phi)\\
\mathcal{C}_\gamma &= -\left(\frac{2\omega_p}{VD}\right)\cos\psi\cos\phi
\end{aligned} \tag{4}$$

Path and Control Constraints

The vehicle has upper limits on dynamic pressure, aerodynamic acceleration, and heat flux. The limit on dynamic pressure is given by

$$\bar{q} = \frac{1}{2}\rho V^2 \leq \bar{q}_{\max} \tag{5}$$

The constraint on aerodynamic acceleration is expressed as

$$L_z = L\cos\alpha + D\sin\alpha \leq A_{\max} \tag{6}$$

Vehicle thermal constraints are treated by using stagnation point heat flux as the sole indicator. The heat flux is constrained according to the heating model

$$\dot{Q} = c\rho^{1/2}V^{3.15} \leq \dot{Q}_{\max} \tag{7}$$

where c is a vehicle-dependent constant.

For drag acceleration guidance methods, the vehicle constraints are converted to an upper drag boundary using the following procedure. First the constraints are converted to separate drag constraints. The dynamic pressure, normal acceleration and heat flux constraints take the forms

$$D \leq \bar{q}_{\max}\frac{S}{m}C_D \tag{8}$$

$$D \leq \frac{A_{\max}}{\sin\alpha + \frac{L}{D}\cos\alpha} \tag{9}$$

$$D \leq \frac{1}{2}\left(\frac{\dot{Q}_{\max}}{cV^{3.15}}\right)^2 V^2\frac{S}{m}C_D \tag{10}$$

Three drag boundary curves are defined by separately treating Eqs. (8–10) as equalities. A composite maximum drag profile, referred to as $D_{\max}$, is constructed by taking the minimum of the three drag boundary values at each energy value. An example of a $D_{\max}$ profile is shown in Fig. 1. The vehicle constraints are met when $D \leq D_{\max}$. The maximum and minimum drag boundaries depend on α. In our approach, the drag profile planning is always performed for a fixed α profile. If the α profile is treated as adjustable in the planning process, then the planning is conducted in a hierarchical manner in which the α profile is adjusted iteratively outside the drag planning, whereas in each cycle the drag is planned with a fixed α profile. If α is commanded for tracking, it is not allowed to differ by more than a few degrees from the profile used for planning.

A lower boundary is also constructed in the D versus E plane, though it is based on vehicle performance capabilities instead of safety-related constraints. The boundary, which we denote $D_{\text{e.g.}}$, is constructed from the zero-bank equilibrium glide condition, which occurs when $\gamma' = 0$ and $\sigma = 0$. A vehicle flying in this condition has just enough lift to maintain its flight path angle. The vehicle cannot maintain steady flight with $D < D_{\text{e.g.}}$. However, flying with $D < D_{\text{e.g.}}$ does not necessarily pose a risk to the vehicle. For this reason the boundary is considered a soft boundary, that is, one that does need not to be enforced strictly. Figure 1 shows an example of a $D_{\text{e.g.}}$ profile.

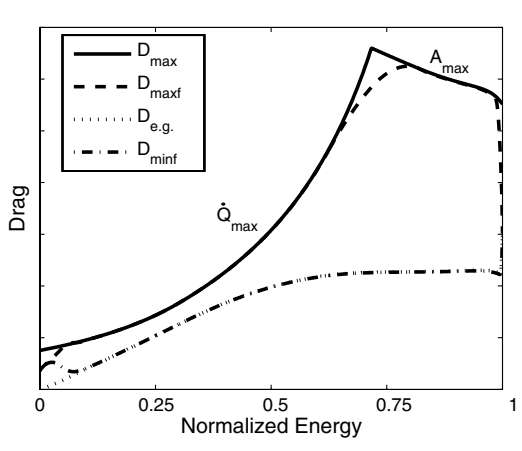

Fig. 1 Drag boundaries.

Limits are placed on the magnitudes of the first and second time derivatives of the σ and α guidance commands according to

$$|\dot{\sigma}| \leq \dot{\sigma}_{\max}, \qquad |\ddot{\sigma}| \leq \ddot{\sigma}_{\max}, \qquad |\dot{\alpha}| \leq \dot{\alpha}_{\max}, \qquad |\ddot{\alpha}| \leq \ddot{\alpha}_{\max} \tag{11}$$

Equation (11) does not necessarily represent vehicle limits. In trajectory planning, more conservative bounds may be used to save capability for tracking.

Target Conditions

The target conditions are application specific. For example, the space shuttle ends its entry phase by starting a terminal area energy management (TAEM) phase, which prepares it for a runway landing. For the computations described in this paper, we adopt the target TAEM initiation point conditions as defined for the advanced guidance and control (AGC) study [10]. Under the conventions of that study, entry terminates at a specified final speed, V_f. The final altitude h_f is specified with a tolerance of ± 3000 ft, the final horizontal distance to the heading alignment cone (HAC) point should be greater than or equal to 27 n miles and less than or equal to 33 n miles, and the final heading angle should be within 5 deg of the line of sight to the HAC point. EAGLE can also be configured for a parachute deployment target. EAGLE handles both cases by targeting a specific point in position space. In the case of targeting for TAEM, the TAEM point, represented as (h_f, θ_f, ϕ_f), is targeted. To meet the final heading requirement, EAGLE changes the location of the TAEM point on the TAEM circle each time it updates the reference trajectory (see [9]). In the case of targeting for parachute deployment conditions, (h_f, θ_f, ϕ_f) is taken as the desired chute deployment point and V_f becomes the chute deployment speed. In both cases, the final altitude h_f is enforced by specifying a final drag value. The accuracy of this method of enforcing h_f depends on the accuracy of the models for density and coefficient of drag.

Entry Guidance Strategy

The objective of an entry guidance algorithm is to solve the entry guidance problem to sufficient accuracy for the set of expected initial and final conditions, despite modeling and navigation errors and delay and inaccuracy in the execution of the guidance commands. We assume that a solution to the guidance problem exists. The task of selecting a feasible entry target (landing site) is not addressed here. In this section we describe the basic features of the guidance strategy employed in EAGLE. EAGLE is composed of a trajectory planner and a trajectory tracker. The trajectory planner features discussed in this section are common to the old and new planner. In the subsequent section, the improved features of the new planner are described and the planning algorithm is given.

Trajectory Planning

EAGLE plans a full 3-DOF trajectory by designing a drag profile and scheduling the bank reversal(s). For the purposes of this paper, we assume that the α profile is given and not to be modified by the planner. (Other work [21,22] by the authors has examined on-board α-profile selection for increased ranging capability. Even if alpha profile selection is part of the planning process, the discussion given here would still apply, due to the hierarchical manner in which the α-profile is adjusted iteratively outside the drag planning.) The first objective in the drag planning is to achieve the downrange of the target. Other constraints, namely the initial and final altitudes and the vehicle constraints, are also enforced during the drag design process. The new planner enforces more constraints, such as limits on $\dot{\sigma}$ and $\ddot{\sigma}$,

as described in the next section. The objective of the bank sign planning is to achieve the crossrange of the target.

For drag planning, the planner creates a family of constraint-observing drag profiles that differ by the value of 1 parameter, P_1. The drag planning entails selecting a value for P_1 that achieves the downrange distance consistent with the target conditions. The parameter associated with the bank sign planning is referred to as P_2. P_2 is the normalized energy at which the primary bank reversal begins. The initial bank sign is chosen to turn the vehicle toward the target. Though other bank reversals may be specified at fixed normalized energy values, they are left fixed and not adjusted by the planner. The selection of P_2 determines the final crossrange, because it is the only free parameter associated with the bank sign profile.

Trajectory Tracking

The purpose of the trajectory tracking function is to command σ and α such that the vehicle follows the reference trajectory produced by the planner. The tracking function accomplishes this by tracking drag, tracking heading angle (though only late in entry), and executing timed bank reversals. Bank angle is treated as the primary control variable. Because the tracking law is also used in the new planning process, we describe it briefly here. For a more complete discussion than is given here, including a description of how limited α commands are issued to control high-frequency drag error in a secondary tracking law, please see [9].

Both the drag tracking law and the heading angle tracking law are based on feedback linearization. The drag tracking law is designed to achieve second-order linear drag error dynamics of the form

$$(D'' - D''_{\text{ref}}) + 2\zeta\omega_n(D' - D'_{\text{ref}}) + \omega_n^2(D - D_{\text{ref}}) + k_1 \int (D - D_{\text{ref}})\,\mathrm{d}E = 0 \tag{12}$$

where ζ is a constant to be tuned, ω_n is scheduled with dynamic pressure, k_1 is a constant gain, and

$$D'' = a + b(L/D)\cos\sigma \tag{13}$$

Variables a and b are functions of the state variables and α that have been given elsewhere [9]. Equation (13) is substituted into Eq. (12), and Eq. (12) is solved for σ at each guidance cycle during entry.

Similarly, the heading tracking law is designed to achieve first-order linear heading angle error dynamics of the form

$$(\psi' - \psi'_{\text{ref}}) + k_2(\psi - \psi_{\text{ref}}) + k_3 \int (\psi - \psi_{\text{ref}})\,\mathrm{d}E = 0 \tag{14}$$

where k_2 is scheduled with dynamic pressure and k_3 is a constant gain. The equation for ψ' [see Eq. (1)], which contains σ, is substituted into Eq. (14), and Eq. (14) is solved for σ at each guidance cycle during entry.

The bank angle command is taken as a weighted combination of the σ values obtained from the two tracking laws. Up until the last part of entry, all of the control weighting is assigned to the drag tracking law. Drag tracking is used exclusively at first because it is challenging and requires full attention. In the absence of modeling error, perfect drag tracking will also result in the reference heading angle being followed perfectly. In actuality, tracking drag exclusively will result in an off-nominal bank command history, causing heading angle to stray from the nominal as well. Planning updates correct the effects of heading error by resetting the timing of the primary bank reversal and starting the reference trajectory from the current heading angle. After the last reversal has been executed, planning updates cannot correct heading error in this manner. For this reason, heading tracking is mixed in at roughly even proportion with drag tracking after the last bank reversal is completed.

New Trajectory Planner

Objectives

The first goal for the new trajectory planner is to be able to plan trajectories that are within the capability of the vehicle to fly, that is, to plan feasible trajectories. A feasible trajectory is one that meets the boundary conditions and the vehicle constraints and that satisfies the equations of motion with the nominal models. The boundary conditions include matching the initial entry state, the initial bank angle σ_0, and the target conditions within certain tolerances. For feasibility as we define it here, we do not require matching the initial angle of attack α_0. Testing of an earlier version of the new planner that did match α_0 led us to conclude that the potential benefits did not justify the increased level of algorithm complexity.

The previous planner designed a three-segment piecewise-linear-in-energy drag profile. The middle segment was taken constant drag. The initial drag value was determined by the initial conditions and the final drag value was determined by the final conditions. The segment breakpoints were chosen to match the shape of the $D_{\max}$ boundary in the D versus E plane. The height of the middle segment was chosen to match a desired trajectory length. Portions of the three-segment drag profile that exceeded $D_{\max}$ were replaced by the corresponding sections of $D_{\max}$. While this method works well over a large part of the entry corridor for orbital entry (it performed well in the AGC study [10]), some problems arise when it is used for suborbital entry. The short duration of suborbital entry makes it harder to correct for the tracking errors that result from infeasibilities in the reference trajectory. Infeasibilities associated with the previous drag design method include not matching σ_0 and γ_0, discontinuous changes in σ and γ at segment breakpoints and at breakpoints introduced by adopting sections of $D_{\max}$, excessive bank angle derivatives, and incompatibility with the γ' equation of Eqs. (1). Arbitrary drag shapes may specify values for γ' that demand more vertical lift than the vehicle can attain by simply lowering $|\sigma|$. Some of the infeasibilities can be quite significant during orbital entry as well, particularly γ' incompatibility, and discontinuities in γ resulting from flying segments of the $D_{\max}$ boundary. The X33-type vehicle model used for the AGC testing had an L/D of about one. Tracking problems for infeasible trajectories will be more serious for lower L/D vehicles, such as capsules.

The second goal for the new trajectory planner is to be able to plan trajectories to the entire landing footprint. The challenging targets not covered by the original EAGLE planner are those near the boundary. These targets are the endpoints of optimal trajectories, yet ideally we would like the planner to compute trajectories to these points without actually solving optimal control problems.

Optimal Trajectory Features

To characterize the features of trajectories to the boundary points of the landing footprint, optimal trajectories were generated using ASTOS,[‡] an optimal control and simulation tool for aerospace applications. ASTOS solves trajectory optimization problems using collocation or direct multiple shooting. The optimization problem we solved is to maximize or minimize the final latitude for a given final longitude θ_f, subject to the initial conditions, equations of motion, constraints, and boundary conditions given earlier. Also, h was constrained to be below h_0 to exclude skip trajectories. The value for θ_f was varied to obtain vertices to construct an optimal landing footprint polygon for a particular initial condition (labeled EG16) given in the performance demonstration section.

The following features of the optimal trajectories were observed and are used to guide the new planner design to increase its crossrange and downrange capabilities. $D(\tilde{E})$ profiles of maximum-range trajectories lie close to the equilibrium glide drag profile, $D_{\text{e.g.}}$, which corresponds to $\gamma' = 0$ and $\sigma = 0$. An example of a $D_{\text{e.g.}}$ profile is shown in Fig. 1. $D(\tilde{E})$ profiles of minimum-range trajectories tend to closely follow the $D_{\max}$ boundary. Maximum crossrange

[‡]ASTOS: AeroSpace Trajectory Optimization Software, http://www.astos.de [cited 10 February 2004].

trajectories show a reduction in drag in the last part of entry, which extends range once the vehicle is headed in the desired direction; with the drag reduction there is a corresponding decrease in the bank angle magnitude and an increase in the vertical component of lift. By imitating these behaviors, the new planner is capable of achieving near-optimal downrange and crossrange.

Feasible Drag Profiles with Optimal Features via Interpolation and Pretracking

The three-segment linear drag profile design of the previous planner is replaced with an interpolation-based feasible drag design method. Drag is taken as a weighted combination of minimum and maximum drag profiles. The interpolation depends on a parameter P_1 defined such that $P_1 = 0$ produces the maximum drag profile, $P_1 = 1$ produces the minimum drag profile, and $0 < P_1 < 1$ produces a drag profile that lies between the two extremes. The use of interpolation is motivated by computation time. During the search for P_1, many drag profiles may be considered. Enforcing feasibility on each profile would increase computation time. Using the interpolation method, direct enforcement of feasibility is required only for the first two profiles that are tested, the lower and upper drag profiles. Our experience indicates that trajectories generated from drag interpolation will be feasible to sufficient accuracy, if both the lower and upper drag profiles are associated with feasible trajectories.

The desired near-optimal behavior is built into the planner in the following manner. The upper drag profile used for interpolation is taken as a feasible variant of the $D_{\max}$ boundary in the D versus E plane, and is referred to as $D_{\max f}$. The lower drag profile is taken as a feasible variant of $D_{\text{e.g.}}$ in the D versus E plane, and is referred to as $D_{\min f}$. Figure 1 shows examples of $D_{\max}$, $D_{\max f}$, $D_{\text{e.g.}}$, and $D_{\min f}$ profiles. The crossrange-enhancing feature is implemented at the interpolation stage of drag design, and is not applied to $D_{\max f}$ or $D_{\min f}$.

The procedures used for generating $D_{\max f}$ and $D_{\min f}$ are basically the same, and so only the procedure for creating $D_{\max f}$ will be described in detail. The trajectory planner creates $D_{\max f}$ by pretracking $D_{\max}$. The term "pretracking" has been used to clarify the point that the tracking is a simulation performed by the planner. The planner performs a tracking simulation and takes the resulting drag history as $D_{\max f}$, a feasible variant of $D_{\max}$. During the simulation, the initial conditions, equations of motion with the nominal models, and control derivative limits are all enforced to ensure that $D_{\max f}$ is feasible. Another control constraint $|\sigma| > \sigma_{\min}$ is enforced (except during bank reversals) to ensure some lateral control authority for tracking. For the results presented in this paper $\sigma_{\min} = 5$ deg. The same feedback linearization (FBL) plus proportional-derivative (PD) drag tracking law used in EAGLE's trajectory tracking function is used to pretrack $D_{\max}$, though the gain tuning is different. For the pretracking, $\zeta = 1$ because an overshoot is not desired. Because of rate saturation of σ, an overshoot in drag may occur if ω_n is too high. A search is performed for the value of ω_n that achieves the closest drag tracking while maintaining the overshoot below a specified tolerance. The overshoot is defined as the maximum value of the drag error, where drag error is $D(E) - D_{\max}(E)$. The tolerance is small but nonzero to allow for minor numerical error effects in the steady-state tracking response. The resulting drag profile is taken as $D_{\max f}$. The search for ω_n is performed by the planner during the creation of the $D_{\max f}$ profile each time a trajectory is planned, though redetermining ω_n each time may not be necessary.

$D_{\max}$ is modified before it is pretracked to create $D_{\max f}$ to smooth the slope discontinuities at energy values where a different vehicle constraint becomes active. Cubic bridging segments are applied at the corners of $D_{\max}$ to give a smooth transition from one constraint curve to the next. A final cubic segment is added to smoothly connect $D_{\max f}$ (not $D_{\max}$) to D_f at the end of entry. The corner cubic segments match the value and slope of $D_{\max}$ at points where they connect to it. The final segment matches the value, slope, and curvature of $D_{\max f}$ at its connection point.

The same procedure is used to create a feasible variant of $D_{\text{e.g.}}$, except that there are no corners in $D_{\text{e.g.}}$ to smooth out. The resulting minimum drag profile is labeled $D_{\min f}$. For low-energy entry conditions or vehicles with low lift to drag ratio, it might be difficult or impossible to attain steady tracking of $D_{\text{e.g.}}$. In these cases $D_{\min f}$ is created by integrating the full equations of motion from the initial entry state with $\sigma = \sigma_{\min}$. This method could always be used to generate $D_{\min f}$, but pretracking $D_{\text{e.g.}}$ is the preferred method when possible because it precludes the excessive phugoiding that can result from flying with $\sigma = \sigma_{\min}$.

In general it is not possible to track $D_{\text{e.g.}}$ with $\sigma = 0$. Experience has shown that tracking $D_{\text{e.g.}}$ requires nonzero σ commands and that γ decreases slowly with time while $D_{\text{e.g.}}$ is tracked. The observation that $\sigma \neq 0$ indicates that $D_{\text{e.g.}}$ is a conservative minimum drag boundary. The conservatism can be removed by multiplying C_L by $1 + \eta$ during the computation of $D_{\text{e.g.}}$, where η is a small number such as 0.05. During the computation of $D_{\min f}$, σ will eventually saturate at $\sigma_{\min}$ and a small phugoid oscillation will occur. The magnitude of the phugoid oscillation decreases as η decreases. The lowest drag profile in Fig. 2c was generated using $\eta = 0.07$. $D_{\text{e.g.}}$ in Fig. 1 was generated with nominal lift ($\eta = 0$). The addition of phugoid motion in this manner increases range. This is consistent with the optimal footprint, whose maximum-range trajectories oscillate slowly near $D_{\text{e.g.}}$. While this modification is important for planning trajectories to the maximum-range boundary of the footprint, it may not be required for planning within an operational guidance algorithm.

Interpolation between $D_{\min f}$ and $D_{\max f}$ is performed according to

$$D(\tilde{E}) = D_{\min f}(\tilde{E}) + \frac{1 - P_1}{1 + e^{k(\tilde{E} - \tilde{E}_m)}}[D_{\max f}(\tilde{E}) - D_{\min f}(\tilde{E})] \quad (15)$$

where P_1 is the normalized downrange parameter and $k > 0$ and $\tilde{E}_m$ are shaping parameters. Equation (15) approximates linear interpolation at values of $\tilde{E}$ sufficiently less than $\tilde{E}_m$. As $\tilde{E}$ increases, drag drops smoothly to $D_{\min f}$. The value of k determines how quickly the transition to $D_{\min f}$ occurs. For the results presented in this paper, $k = 30$ and $\tilde{E}_m = 0.85$. Drag is reduced at the end of entry to increase crossrange, imitating this feature observed in the optimal trajectories. As it is, Eq. (15) does not produce $D_{\max f}$ when $P_1 = 0$ because of the crossrange-enhancing drag reduction at the end. The equation can be modified to gradually eliminate the drag reduction as P_1 approaches 0. One way to do this is to replace P_1 with $\max(1.2P_1 - 0.2, 0)$ and $\tilde{E}_m$ with $\tilde{E}_m - 2\min(1.2P_1 - 0.2, 0)$ in the equation. Figure 2 gives an example of drag profiles generated using Eq. (15) with the substitutions. For low-energy cases, including the suborbital cases of the AGC study [10], the total entry time is not sufficient for the drag reduction method that has been described to be an effective means of increasing crossrange. In these cases, simple linear interpolation is applied according to

$$D(\tilde{E}) = P_1 D_{\min f}(\tilde{E}) + (1 - P_1) D_{\max f}(\tilde{E}) \quad (16)$$

Experience has shown that the bank angle profiles that result from the drag interpolation of Eqs. (15) and (16) are flyable when $D_{\max f}$ and $D_{\min f}$ are both flyable and appropriate values for k and $\tilde{E}_m$ are used for Eq. (15).

Feasible Bank Reversal Planning

In order for a trajectory to be feasible, bank sign reversals cannot occur instantaneously. A trajectory is modified to include a rate-limited bank reversal in the following manner. Starting from the value of $\tilde{E}$ where the reversal is scheduled to begin, the equations of motion are integrated using an open-loop constant rate bank reversal. After the reversal is complete, pretracking with the FBL plus PD drag tracking law is used to smoothly return the drag to the original curve. As during the computation of $D_{\max f}$ and $D_{\min f}$, $\zeta = 1$ is used along with the highest value of ω_n that maintains the overshoot below a small tolerated value. As before, the planner finds this value through

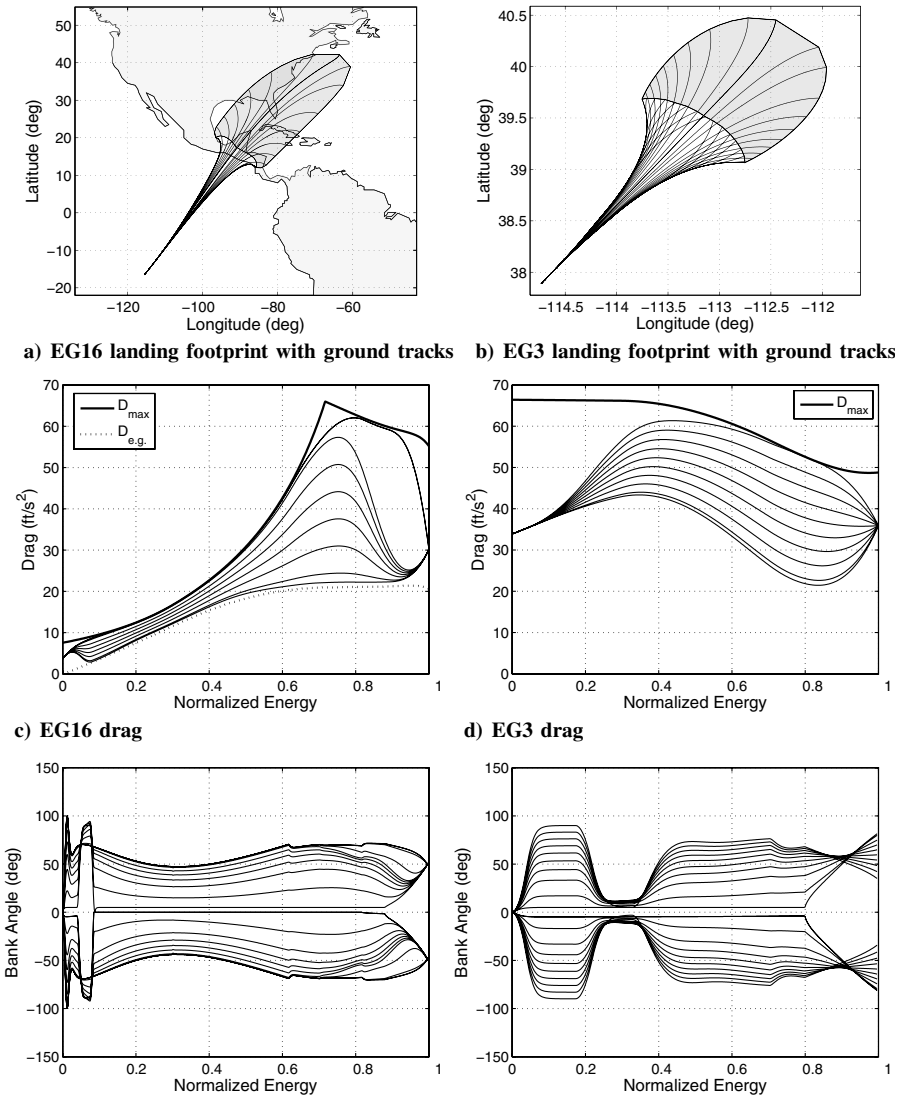

a) EG16 landing footprint with ground tracks
b) EG3 landing footprint with ground tracks
c) EG16 drag
d) EG3 drag
e) EG16 bank angle
f) EG3 bank angle

Fig. 2 Trajectories from the new planner.

an automated numerical search. The pretracking simulation is terminated once the drag error and the drag slope error are both below specified tolerances.

For low and medium crossrange entry scenarios, a second bank reversal is added near the end of entry to reserve some crossrange correction capability. In planning updates that occur before the first reversal is executed, the normalized energy at which the second reversal occurs is fixed. In these initial updates, P_2 controls the first bank reversal. After the first reversal has been executed, P_2 controls the remaining bank reversal. Unless an additional reversal is allowed, it is important that the second bank reversal is planned to occur near the target, because after it is executed, the planner loses its ability to target in crossrange. For entry cases that require high crossrange or for low-energy cases, a single bank reversal is sufficient if it will occur close enough to the target. The previous planner scheduled the two bank reversals in a slightly different manner, to similar effect [9]. However, the new method that is described here eliminates one of the two parameters that were previously associated with adding a second bank reversal.

Planning Algorithm

The function of the planning algorithm is to generate a feasible entry trajectory. We have parameterized the final longitude and latitude with the parameters P_1 and P_2. The parameter $P_1 \in [0, 1]$ specifies the drag profile; the parameter $P_2 \in [0, 1]$ specifies the bank reversal initiation normalized energy. The target longitude and latitude values are denoted by (θ_f, ϕ_f). For the evaluation of the delivery error in longitude and latitude, the final position is expressed in "target frame" coordinates. The final 3D position is projected radially onto the sphere of radius r_f, where r_f is the target radius. The distance along the great circle containing the target final position, which is on this sphere, and the projected initial position is defined as downrange; whereas the crossrange distance for a given downrange is measured along the great circle, on the same sphere that intersects the downrange great circle perpendicularly. The downrange distance error is denoted by e_{dr}, with a positive value denoting an overshoot, the crossrange distance error by e_{cr}, with a positive value denoting an error to the right of the downrange great circle. Accordingly, we write $e_{\mathrm{dr}}(P_1, P_2)$ and $e_{\mathrm{cr}}(P_1, P_2)$.

The problem solved by the planning algorithm is thus to determine (P_1, P_2) such that $e_{\mathrm{dr}}(P_1, P_2) = 0$ and $e_{\mathrm{cr}}(P_1, P_2) = 0$. The inputs to the algorithm are the boundary conditions on the state, the final energy E_f, the path constraint bounds $\bar{q}_{\max}$, $A_{\max}$, and $\dot{Q}_{\max}$, a reference α profile, nominal models for C_D, ρ, and g, and tolerances $\mathrm{TOL}_{\mathrm{dr}}$ and $\mathrm{TOL}_{\mathrm{cr}}$ for the downrange and crossrange errors. A successive approximation approach is used to determine the (P_1, P_2) pair that nulls the downrange and crossrange errors. P_1 is adjusted in an outer-loop false position search to achieve the target downrange. Each time P_1 is updated during the search, an inner loop determines the value of P_2 that minimizes the crossrange error. With this successive approximation approach, P_1 and P_2 are found using

"nested" single-parameter searches instead of a two-parameter search. The false position searches converge to within an acceptable tolerance after several iterations. Approximately 50 to 100 (P_1, P_2) pairs are tested during the process, which takes less than 2 s on current desktop computing hardware.

We first describe two key components of the algorithm—the false position search and the mapping from (P_1, P_2) to $e_{dr}(P_1, P_2)$ and $e_{cr}(P_1, P_2)$—then we describe the algorithm.

False Position Search: For a scalar function $f(x)$, the problem is to determine c such that $f(c) = 0$ given a priori information that $c \in [a_0, b_0]$ and $\text{sgn}[f(a_0)] = -\text{sgn}[f(b_0)]$. The update equation is

$$c_k = \frac{a_k f(b_k) - b_k f(a_k)}{f(b_k) - f(a_k)} \tag{17}$$

If $\text{sgn}[f(a_k)] = \text{sgn}[f(c_k)]$, then $(a_{k+1}, b_{k+1}) = (c_k, b_k)$; otherwise, $(a_{k+1}, b_{k+1}) = (a_k, c_k)$. The search is initialized with $k = 0$ and continued until the iteration l when $|f(c_l)| < \text{TOL}$ is first satisfied, for a specified tolerance TOL. This search only has linear convergence, but we have found it to perform reliably.

Mapping: $(P_1, P_2) \rightarrow e_{dr}(P_1, P_2)$ and $e_{cr}(P_1, P_2)$

1) Compute $r(E)$, $V(E)$, and $\gamma(E)$, and $L\cos(\sigma)$ from $D(E)$ and $\alpha(E) - r(E)$ from the second of Eqs. (2) and the nominal models for C_D and ρ, $V(E)$ from E and r, $\gamma(E)$ from the third of Eqs. (1) and a finite-difference approximation of $r'(E)$, and $L\cos\sigma$ from the fifth of Eqs. (1) with $C_\gamma = 0$.

2) Integrate the first, second, and fourth of Eqs. (1) using the $D(E)$, $\alpha(E)$, $r(E)$, $\gamma(E)$, $V(E)$, and $L\cos\sigma$ profiles, with $L\cos\sigma$ corrected at each integration step to account for C_γ. The magnitude of the lateral lift component is obtained as $|L\sin\sigma| = [L^2 - (L\cos\sigma)^2]^{1/2}$; the initial sign of the lateral lift component is selected so that the vehicle will turn toward the target, and a bank reversal is initiated at the normalized energy $\tilde{P}_2$ and handled as already described.

This procedure generates the complete entry trajectory; in particular, it generates values of $e_{dr}(P_1, P_2)$ and $e_{cr}(P_1, P_2)$.

Planning Algorithm:

1) Compute $D_{\min_f}$ and $D_{\max_f}$ and use either Eqs. (15) or (16) to establish the P_1 parametrization. If Eq. (15) is used, the parameters k and $\tilde{E}_m$ must be specified.

2) Outer-loop false position search for P_1 such that $e_{dr}(P_1, P_2) = 0$: the initial bounding values are 0 and 1, that is, $(a_0, b_0) = (0, 1)$; subsequently P_1 is updated according to Eq. (17) with $f(P_1) = e_{dr}(P_1, P_2)$. The iterative search is stopped when $|e_{dr}(P_1, P_2)| < \text{TOL}_{dr}$.

3) Inner-loop search for P_2 such that $|e_{cr}(P_1, P_2)|$ is minimized with P_1 fixed at the current value in the outer-loop search. If $\text{sgn}[e_{cr}(P_1, 0)] = \text{sgn}[e_{cr}(P_1, 1)]$, then $P_2 = 1$ is the minimizing value. Physically this is the case where the initial bank angle sign, chosen such that the vehicle is turning toward the target, remains appropriate for the whole trajectory. Because, with the given drag profile (determined by the value of P_1), the vehicle cannot achieve $e_{cr} = 0$. If, on the other hand, $\text{sgn}[e_{cr}(P_1, 0)] = -\text{sgn}[e_{cr}(P_1, 1)]$, then execute a false position search for the value of P_2 that nulls $f(P_2) = e_{cr}(P_1, P_2)$. The search is initialized with $(a_0, b_0) = (0, 1)$ and is stopped when $|e_{cr}(P_1, P_2)| < \text{TOL}_{cr}$.

Similarities and Differences with Shuttle Approach

This algorithm is drag based like the Shuttle approach. This features eases the handling of path constraints and limits the prediction sensitivity to phugoidlike motion. The vertical plane dynamics for r and γ are not integrated, except in the pretracking procedure to generate $D_{\min_f}$ and $D_{\max_f}$, and to shape the transient following a bank reversal, where the phugoidlike motion is controlled by feedback. In contrast to the Shuttle approach, 1) rather than assuming r is constant and $\gamma = 0$, r, and γ are deduced from D, 2) the lateral motion is accounted for and a bank reversal is planned, 3) a feasible trajectory is planned, and 4) trajectories to most points in the landing footprint can be planned.

Performance Demonstrations

In this section the performance of the planner is demonstrated: first for landing footprint generation and second in the role of the planning function in EAGLE. For the purpose of these demonstrations, logic for deciding whether the case is high or low-energy, or high or low-medium crossrange and executing the appropriate planning technique has not been automated in the planning algorithm we use. Development of a stand alone algorithm and validation via extensive simulation testing is outside the scope of this paper.

The results presented here are based on the vehicle model and initial entry conditions from the advanced guidance and control (AGC) project [10], but using our own simulation rather than the one used in the AGC project. The vehicle model is an enhanced model of the X-33. In the AGC testing for entry guidance, there were 9 orbital entry cases, labeled EG13 to EG21, and 19 suborbital cases labeled EG1 to EG12 and EG22 to EG28. Six of the 9 orbital cases test the high-crossrange guidance capability of the algorithms involved with respect to the baseline guidance algorithm, which was modeled after the Shuttle entry guidance [2]. The suborbital cases test the ability of the algorithms to deal with abort situations, including several involving mismodeling and actuator failures. EAGLE, with its original planner, was submitted for testing in the AGC project and scored well overall [9,10,21]. Though EAGLE tested exceptionally well for all of the orbital cases, the scores were lower for several of the suborbital cases. This is due in large part to the factors that have motivated the development of the new planner.

The new planner is first demonstrated by using it for landing footprint generation. The set of final downrange and crossrange points that a planner can target for a given entry state is an approximation of the vehicle's landing footprint. The accuracy of the approximation depends on the planner that is used. By comparing the planner-generated footprints with the actual footprints, computed by trajectory optimization, one can determine how much of the actual footprint the planner is capable of covering.

To create a landing footprint, the mapping function of the new EAGLE planner is called repeatedly with varying values specified for P_1 and P_2. (No iteration to determine P_1 and P_2 is required, because there is no prespecified target.) The endpoints of the resulting trajectories serve as the vertices of a polygon that represents the footprint approximation. The footprint has four basic sides, each a constant P_1 or P_2 curve (a piecewise linear curve due to the finite number of vertices), as diagrammed in Fig. 3. In the figure, sides B and D correspond to maximum crossrange ($P_2 = 1$), side C corresponds to maximum downrange ($P_1 = 1$), and side A corresponds to minimum downrange ($P_1 = 0$). Positive-crossrange trajectories are generated with a positive initial bank sign and negative-crossrange trajectories are created with a negative initial bank sign. (For entry guidance, only one initial bank sign is used: the one that initially turns the vehicle toward the target.)

Figures 2a and 2b show EAGLE-generated landing footprints for the EG3 and EG16 initial conditions. Ground tracks are shown in Figs. 2a and 2b for every third vertex of those that make up the

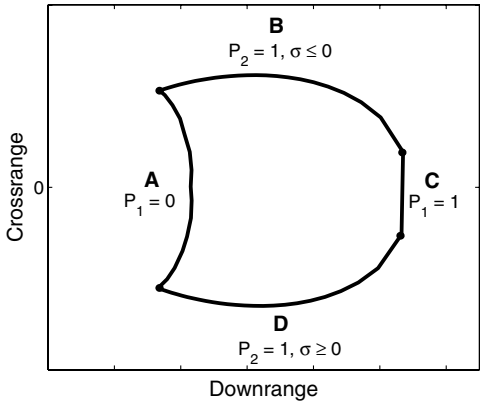

Fig. 3 Landing footprint diagram.

footprint border polygons. Figures 2c and 2d show the drag profiles that correspond to the side boundary trajectories shown in Figs. 2a and 2b, respectively. In Fig. 2c, the drag profile just below $D_{\max}$ is $D_{\max f}$, and the profile just above $D_{\text{e.g.}}$ is $D_{\min f}$. The interior profiles are obtained by interpolation according to Eq. (15) with the substitutions for P_1 and $\tilde{E}_m$ described in the previous section. In Fig. 2d, the drag profile just below $D_{\max}$ is $D_{\max f}$, and the lowest profile is $D_{\min f}$. $D_{\text{e.g.}}$ is not shown because $D_{\min f}$ was obtained from $\sigma = \sigma_{\min}$. The interior profiles are obtained by interpolation according to Eq. (16). Note that all of the drag profiles of the same plot start at the same value and slope and end at the same value, which comes from the planner matching V_0, h_0, γ_0, V_f, and h_f. In Fig. 2c, $D_{\min f}$ is slightly above $D_{\text{e.g.}}$ once it levels out. This is because $D_{\text{e.g.}}$ was calculated with an exaggerated lift coefficient, for reasons that were explained in the previous section.

Figures 2e and 2f show the bank profiles that are associated with the trajectories to the side boundary shown in Figs. 2a and 2b, respectively. The highest-magnitude bank profile in each subfigure corresponds to the $D_{\max f}$ profile, and the lowest-magnitude bank profile in each subfigure corresponds to the $D_{\min f}$ profile. The drop in $|\sigma|$ that is seen in the $D_{\max f}$ bank profiles of Fig. 2f occurs because $D_{\max f}$ is obtained through the pretracking of $D_{\max}$ by the planner. When $D_{\max f}$ gets near $D_{\max}$, the reduction in $|\sigma|$ causes $D_{\max f}$ to level out. The bank profiles indicate the feasibility of the trajectories. They observe the limits on $|\dot{\sigma}|$ and $|\ddot{\sigma}|$ of 10 deg/s and 2 deg/s^2, respectively, and match $\sigma_0 = 0$, the initial bank angle.

Figure 4 shows the boundary of the optimal landing footprint for the EG16 initial entry state. The EAGLE footprint is shown in the figure as a transparent filled polygon. The EAGLE footprint is a close approximation of the optimal footprint. The optimal footprint achieves slightly greater downrange, due to the phugoidlike oscillatory motion that is seen in the optimal minimum drag profile (not shown here), in which D oscillates around $D_{\text{e.g.}}$. The initial undershooting of $D_{\text{e.g.}}$ is the main explanation for the extra range. Phugoiding after the initial undershoot does not completely balance out the extra range because the magnitude of the oscillation decreases steadily with time.

Because of the ability to plan feasible reference trajectories, the suborbital guidance performance of EAGLE with the new planner has improved considerably. Figure 5 shows a tracking simulation for

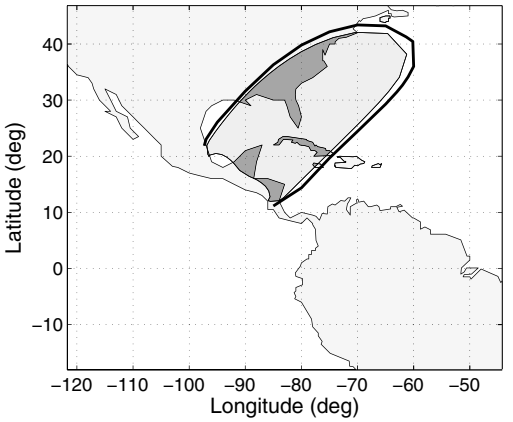

Fig. 4 EG16 landing footprint shown inside of optimal footprint.

the EG3 initial condition. The vehicle starts relatively close to the target, providing little time for the drag tracking to eliminate transients that would occur from the infeasibilities associated with the previous trajectory planner. As such, EG3 is a good case for demonstrating EAGLE with its new trajectory planner. Modeling errors are added to C_L, C_D, and ρ. EAGLE uses the nominal models, whereas perturbed versions are used in the simulation. A sinusoidal multiplicative error with low frequency is applied to C_D and C_L, with Mach number as the independent variable. In the simulation, the nominal C_D is multiplied by $1.025 + 0.025\sin(M + 4.57)$, C_L is multiplied by $0.975 + 0.025\cos(M + 4.57)$, and ρ is multiplied by 0.95. The simulation is 3-DOF, and the commanded control values are low-pass filtered to simulate the presence of an entry flight control system. The filter delays the bank angle and angle of attack commands by about 1 s. Figure 5a shows the drag tracking response. D starts below D_{ref} because α starts below α_{ref} (Fig. 5c). A discontinuous jump in the $D_{\min f}$ boundary occurs at 50 sec, indicating that the reference trajectory was updated at that time. This is expected because updates were scheduled to occur automatically every 50 sec. The discontinuity occurs because $D_{\min f}$ starts from the current reference state at a trajectory update. The tracking proves to be close enough for the final condition error tolerances. A three-segment linear-in-energy drag profile could not have been followed

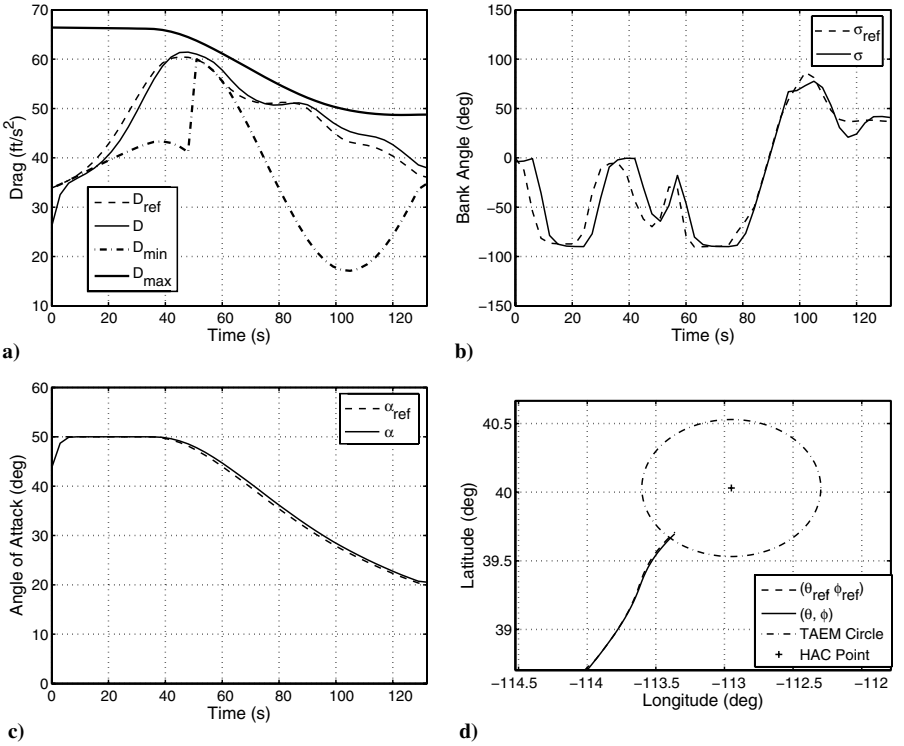

Fig. 5 EG3 guidance simulation.

as closely. Figure 5b shows the commanded and reference bank angle profiles. One bank reversal can be seen to start at $t = 80$ s. Figure 5d shows approximately the second half of the ground track. The final range-to-HAC error is -2.2 n miles, which falls within the 3 n mile AGC project tolerance. The final heading-to-HAC error is -2.8 deg, which falls within the 5 deg AGC project tolerance. The final altitude error is -1300 ft, which falls within the 3000 ft AGC project tolerance. It should be noted that, though the final conditions fall within AGC tolerances, the test environment that we used was not the same as in the AGC study; and thus our results do not necessarily indicate how the algorithm would perform in that test environment.

Orbital tracking results are not shown due to space limitations, but the use of the new planner does not have a large impact on EAGLE's performance for the 9 orbital AGC cases, which was already very good. The previous planner produced trajectories that were sufficiently close to being feasible for AGC13 to AGC21, and so the tracking function was able to compensate in those cases. For orbital entry, the new planner will have the largest impact on entry scenarios involving extreme downrange or crossrange targets that it can reach but the previous planner could not, and on scenarios where the previous planner would have created drag profiles that require unattainable values for γ'.

In all cases, landing footprint computation and trajectory planning took between 1 and 2 s (coded in C) on a Pentium 4, 2.8 GHz personal computer. For the trajectory planning results in this paper, the tolerances for terminating the successive approximation iterations were 3000 ft for downrange and 1000 ft for crossrange. Because much of the computation time is associated with determining $D_{\max f}$ and $D_{\min f}$, the computation time is not strongly dependent on the values of the tolerances. For example, tightening the downrange tolerance to 0.03 ft doubled the number of iterations required but the total computation time only increased from 1.63 to 1.95 s.

Conclusions

An atmospheric entry trajectory planner has been developed that generates a feasible trajectory and associated bank angle profile. Feasibility ensures that the initial and final state conditions, the path and control constraints, and the nominal equations of motion are all satisfied. Feasible trajectories are easier to track; control saturation is less likely, as are path constraint violations. Guidance simulation results using an algorithm based on the planner demonstrated the performance improvements. Insights from computing maximum crossrange trajectories were factored into the design of the planner. Comparisons of trajectories created by the planner and optimal trajectories demonstrated that the planner can generate trajectories to most of the landing footprint. This result is especially significant considering the planner's fast computation time.

Acknowledgments

The research described in this paper was supported in part by the Jet Propulsion Laboratory, California Institute of Technology under contract with the National Aeronautics and Space Administration. The first author gratefully acknowledges support from Graduate Assistance in Areas of National Need (GAANN) and Holmes fellowships. We thank the Associate Editor and the anonymous reviewers; their comments led to improvements in the paper.

References

[1] Hanson, J. M., "New Guidance for New Launchers," *Aerospace America*, Vol. 41, No. 3, 2003, pp. 36–41.

[2] Harpold, J. C., and Graves, C. A., Jr., "Shuttle Entry Guidance," *Journal of the Astronautical Sciences*, Vol. 27, No. 3, 1979, pp. 239–268.

[3] Roenneke, A. J., and Markl, A., "Re-entry Control of a Drag vs Energy Profile," *Journal of Guidance, Control, and Dynamics*, Vol. 17, No. 5, 1994, pp. 916–920.

[4] Lu, P., "Entry Guidance and Trajectory Control for Reusable Launch Vehicle," *Journal of Guidance, Control, and Dynamics*, Vol. 20, No. 1, 1997, pp. 143–149.

[5] Lu, P., and Hanson, J. M., "Entry Guidance for the X-33 Vehicle," *Journal of Spacecraft and Rockets*, Vol. 35, No. 3, 1998, pp. 342–349.

[6] Tu, K.-Y., Munir, M. S., Mease, K. D., and Bayard, D. S., "Drag-Based Predictive Tracking Guidance for Mars Precision Landing," *Journal of Guidance, Control, and Dynamics*, Vol. 23, No. 4, 2000, pp. 620–628.

[7] Grimm, W., van der Meulen, J. G., and Roenneke, A. J., "Optimal Update Scheme for Drag Reference Profiles in an Entry Guidance," *Journal of Guidance, Control, and Dynamics*, Vol. 26, No. 5, 2003, pp. 695–701.

[8] Mease, K. D., Chen, D. T., Teufel, P., and Schönenberger, H., "Reduced-Order Entry Trajectory Planning for Acceleration Guidance," *Journal of Guidance, Control, and Dynamics*, Vol. 25, No. 2, 2002, pp. 257–266.

[9] Saraf, A., Leavitt, J. A., Chen, D. T., and Mease, K. D., "Design and Evaluation of an Acceleration Guidance Algorithm for Entry," *Journal of Spacecraft and Rockets*, Vol. 41, No. 6, 2004, pp. 986–996.

[10] Hanson, J. M., and Jones, R. E., "Test Results for Entry Guidance Methods for Space Vehicles," *Journal of Guidance, Control, and Dynamics*, Vol. 27, No. 6, 2004, pp. 960–966.

[11] Shen, Z., and Lu, P., "Onboard Generation of Three-Dimensional Constrained Entry Trajectories," *Journal of Guidance, Control, and Dynamics*, Vol. 26, No. 1, 2003, pp. 111–121.

[12] Shen, Z., and Lu, P., "Dynamic Lateral Entry Guidance Logic," *Journal of Guidance, Control, and Dynamics*, Vol. 27, No. 6, 2004, pp. 949–959.

[13] Jouhaud, F., "Closed Loop Reentry Guidance Law of a Space Plane: Application to Hermes," *Acta Astronautica*, Vol. 26, Nos. 8–10, 1992, pp. 577–585.

[14] Youssef, H., Chowdhry, R., Lee, H., Rodi, P., and Zimmerman, C., "Predictor–Corrector Entry Guidance for Reusable Launch Vehicles," *Guidance, Navigation, and Control Conference and Exhibit, Montreal, Canada*, AIAA Paper 2001-4043, August 2001.

[15] Dukeman, G. A., "Profile-Following Entry Guidance Using Linear Quadratic Regulator Theory," AIAA Paper 2002-4457, August 2002.

[16] Zimmerman, C., Dukeman, G. A., and Hanson, J. M., "Automated Method to Compute Orbital Reentry Trajectories with Heating Constraints," *Journal of Guidance, Control, and Dynamics*, Vol. 26, No. 4, 2003, pp. 523–529.

[17] Shen, Z., and Lu, P., "Onboard Entry Trajectory Planning Expanded to Sub-Orbital Flight," AIAA Paper 2003-5736, August 2003.

[18] Powell, R. W., "Six-Degree-of-Freedom Guidance and Control Entry Analysis of the HL-20," *Journal of Spacecraft and Rockets*, Vol. 30, No. 5, 1993, pp. 537–542.

[19] Mendeck, G. F., and Carman, G. L., "Guidance Design for Mars Smart Landers Using the Entry Terminal Point Controller," AIAA Paper 2002-4502, August 2002.

[20] Vinh, N. X., *Optimal Trajectories in Atmospheric Flight*, Elsevier, New York, 1981.

[21] Saraf, A., Leavitt, J. A., Chen, D. T., and Mease, K. D., "Design and Evaluation of an Acceleration Guidance Algorithm for Entry," AIAA Paper 2003-5737, August 2003.

[22] Saraf, A., Leavitt, J. A, Ferch, M., and Mease, K. D., "Landing Footprint Computation for Entry Vehicles," AIAA Paper 2004-4774, August 2004.